

PAPER • OPEN ACCESS

Activation of retinal ganglion cells using a biomimetic artificial retina

To cite this article: Jordan A Greco *et al* 2021 *J. Neural Eng.* **18** 066027

View the [article online](#) for updates and enhancements.

You may also like

- [Simulation and performance of an artificial retina for 40 MHz track reconstruction](#)
A. Abba, F. Bedeschi, M. Citterio et al.
- [Electrophysiological investigation of intact retina with soft printed organic neural interface](#)
Ieva Vbrait, Moshe David-Pur, David Rand et al.
- [An artificial retina processor for track reconstruction at the LHC crossing rate](#)
F Bedeschi, R Cenci, P Marino et al.



PAPER

OPEN ACCESS

RECEIVED

26 May 2021

REVISED

10 November 2021

ACCEPTED FOR PUBLICATION

12 November 2021

PUBLISHED


1 December 2021

Original content from this work may be used under the terms of the [Creative Commons Attribution 4.0 licence](#).

Any further distribution of this work must maintain attribution to the author(s) and the title of the work, journal citation and DOI.



Activation of retinal ganglion cells using a biomimetic artificial retina

Jordan A Greco¹ , Nicole L Wagner^{1,2}, Ralph J Jensen³, Daniel B Lawrence⁴, Matthew J Ranaghan², Megan N Sandberg¹, Daniel J Sandberg¹ and Robert R Birge^{1,2,*}

¹ Department of Chemistry, University of Connecticut, 55 North Eagleville Road, Storrs, CT 06269, United States of America

² Department of Molecular and Cell Biology, University of Connecticut, 91 North Eagleville Road, Storrs, CT 06269, United States of America

³ VA Boston Healthcare System, 150 South Huntington Avenue, Boston, MA 02130, United States of America

⁴ University of Connecticut School of Medicine, 263 Farmington Avenue, Farmington, CT 06032, United States of America

* Author to whom any correspondence should be addressed.

E-mail: rbirge@uconn.edu

Keywords: protein-based artificial retinas, retinal degeneration, retinitis pigmentosa, visual restoration, bacteriorhodopsin, layer-by-layer assembly, acid-sensing ion channels

Supplementary material for this article is available [online](#)

Abstract

Objective. Biomimetic protein-based artificial retinas offer a new paradigm for restoring vision for patients blinded by retinal degeneration. Artificial retinas, comprised of an ion-permeable membrane and alternating layers of bacteriorhodopsin (BR) and a polycation binder, are assembled using layer-by-layer electrostatic adsorption. Upon light absorption, the oriented BR layers generate a unidirectional proton gradient. The main objective of this investigation is to demonstrate the ability of the ion-mediated subretinal artificial retina to activate retinal ganglion cells (RGCs) of degenerated retinal tissue. **Approach.** *Ex vivo* extracellular recording experiments with P23H line 1 rats are used to measure the response of RGCs following selective stimulation of our artificial retina using a pulsed light source. Single-unit recording is used to evaluate the efficiency and latency of activation, while a multielectrode array (MEA) is used to assess the spatial sensitivity of the artificial retina films. **Main results.** The activation efficiency of the artificial retina increases with increased incident light intensity and demonstrates an activation latency of ~150 ms. The results suggest that the implant is most efficient with 200 BR layers and can stimulate the retina using light intensities comparable to indoor ambient light. Results from using an MEA show that activation is limited to the targeted receptive field. **Significance.** The results of this study establish potential effectiveness of using an ion-mediated artificial retina to restore vision for those with degenerative retinal diseases, including retinitis pigmentosa.

1. Introduction

Retinitis pigmentosa (RP) is the most common form of heritable retinal degeneration, affecting approximately 1.5 million people globally (1 in ~4000 individuals) (Berson 1996). This disorder is characterized by the progressive degeneration of photoreceptor cells resulting from a diverse group of genetic defects linked to key biological aspects of cellular structure and function of the retina (Verbakel *et al* 2018). For most occurrences of RP, rod cell degeneration first causes night blindness and tunnel vision, which leads

to the subsequent loss of cone cells (Wang *et al* 2016) and eventual end-stage degeneration where only bare light perception is possible. Some inner transsynaptic degeneration and remodeling occurs following photoreceptor degeneration (Marc *et al* 2003), though the bipolar and ganglion cell networks often remain viable when advanced RP has been reached (Humayun *et al* 1999).

Treatments under development for advanced stages of RP presenting significant photoreceptor degeneration include retinal prosthetics (Humayun *et al* 2012, Lorach *et al* 2015), exogenous chemical

photoswitches (Tochitsky *et al* 2014), or optogenetic tools (Bi *et al* 2006, Sahel *et al* 2021). These methods allow for the photosensitization and stimulation of extant networks in the retina, and can exploit the processing, amplification, and encoding offered by 2nd- and 3rd-order retinal neurons. These treatment approaches could be effective regardless of the genetic origin of the disease. Prosthetic microelectronic technologies have had the most significant clinical impact to date, though prominent early technologies with successful market authorizations, including the Argus II (Second Sight) (Humayun *et al* 2012, Luo and Da Cruz 2016) and the Alpha IMS/AMS (Retina Implant AG) (Stingl *et al* 2015, 2017) technologies, have been discontinued. More recently, a wireless photovoltaic retinal implant (PRIMA; Pixium Vision, Inc.) has shown promise in treating advanced atrophic dry age-related macular degeneration (Palanker *et al* 2020). Optogenetic approaches utilize exogenous microbial rhodopsins (e.g. cation-conducting channelrhodopsin-2 (Nagel *et al* 2003), anion-conducting halorhodopsin (Bamberg *et al* 1993), or proton-pumping proteins (Chow *et al* 2010)) to control cell membrane potentials in neurons to restore vision (Kandori 2020). Multiple clinical trials are in progress to examine the safety and efficacy of optogenetic technologies, including RST-001 (Allergan; NCT02556736), a gene therapy treatment that leads to the expression of channelrhodopsin-2 in retinal ganglion cells (RGCs) of patients with advanced RP.

The artificial retina discussed herein uses bacteriorhodopsin (BR), the archaeal type I rhodopsin from *Halobacterium salinarum* (*H. salinarum*), to replace photoreceptor cells by absorbing light and generating a proton gradient to activate degenerated retinas (Chen and Birge 1993). Despite a significantly different biological role than type II rhodopsins (e.g. mammalian visual pigments) (Birge 1981), type I and type II rhodopsins share several structural and functional features (Devine *et al* 2013) and a nearly identical quantum efficiency (~65%) (Govindjee *et al* 1990). BR contains a covalently-linked chromophore, all-trans retinal, which absorbs incident light ($400 < \lambda < 660$ nm), undergoes isomerization to 13-cis retinal, and initiates a series of proton translocation events (the BR photocycle) (Bogomolni *et al* 1976). The result of the photocycle is the net translocation of a proton from the intracellular to the extracellular domain of the protein in roughly 10 ms.

Trimers of BR are arranged within a 2D crystal-line lattice in the native lipid environment, which is conventionally known as the purple membrane (PM) (Blaurock and Stoerkenius 1971). The highly stable PM structure is able to withstand temperatures up to 80 °C (Jackson and Sturtevant 1978), and the cyclicality of the protein (i.e. the number of photocycles before the sample degrades by $1/e$) exceeds 10^6 cycles (Birge 1990). Moreover, the PM

can maintain function following exposure to diverse chemical environments, including a broad pH range ($3 < \text{pH} < 10$) (Balashov 2000) and encapsulation in non-native polymer matrices (Birge *et al* 1999). The protein can also undergo functional enhancements through the use of mutagenesis (Wagner *et al* 2013), synthetic retinal analogs (Singh and Hota 2007), and lipid modifications (Berthoumieu *et al* 2012). The photochemistry and stability of BR has led to the development of numerous bioelectronic applications (Birge *et al* 1999, Hampp 2000).

In this study, we describe a protein-based artificial retina technology that is at the intersection of implantable electrode-based prosthetics and optogenetic therapies, in which the microbial rhodopsin and proton pump, BR, is integrated into a multilayered film that can stimulate retinal neural cells (Chen and Birge 1993). The high optical density of the multilayered BR-based artificial retina circumvents the low expression levels and high light intensity requirements of optogenetic techniques by mimicking the native layering of the rhodopsin-containing disk membranes within the outer segments of rod and cone cells. The artificial retina architecture discussed herein is enabled by a layer-by-layer (LBL) electrostatic adsorption approach (He *et al* 1998) that is used to generate highly uniform films that can create a unidirectional proton gradient. Oriented BR-based thin films have previously demonstrated edge enhancement and motion detection in an *in vitro* setting (Miyasaka *et al* 1992), thus offering promise to mimic the differential responsivity characteristics of mammalian photoreceptor cells (Chen and Birge 1993). Subretinal layers of unidirectionally-oriented BR are used to establish a proton gradient towards the bipolar and ganglion cells of the degenerated retinas of P23H line 1 rats. Extracellular recording experiments with P23H line 1 rat retinas are used to evaluate the activity and spatiotemporal characteristics of this multi-laminated artificial retina. The results presented in this study provide preliminary evidence of an alternative ion-mediated biomimetic approach for visual restoration following retinal degeneration.

2. Methods

2.1. Chemicals and buffers

All chemicals were purchased from ThermoFisher Scientific (Pittsburg, PA) or Sigma-Aldrich (St Louis, MO). Mesh polyethylene terephthalate (PET) films (i.e. Dacron®) used to create the artificial retinas were received from Goodfellow Corporation (Coraopolis, PA).

2.2. Strain generation, protein isolation, and purification

BR is a seven trans-membrane α -helical proton pump that is expressed in its native organism,

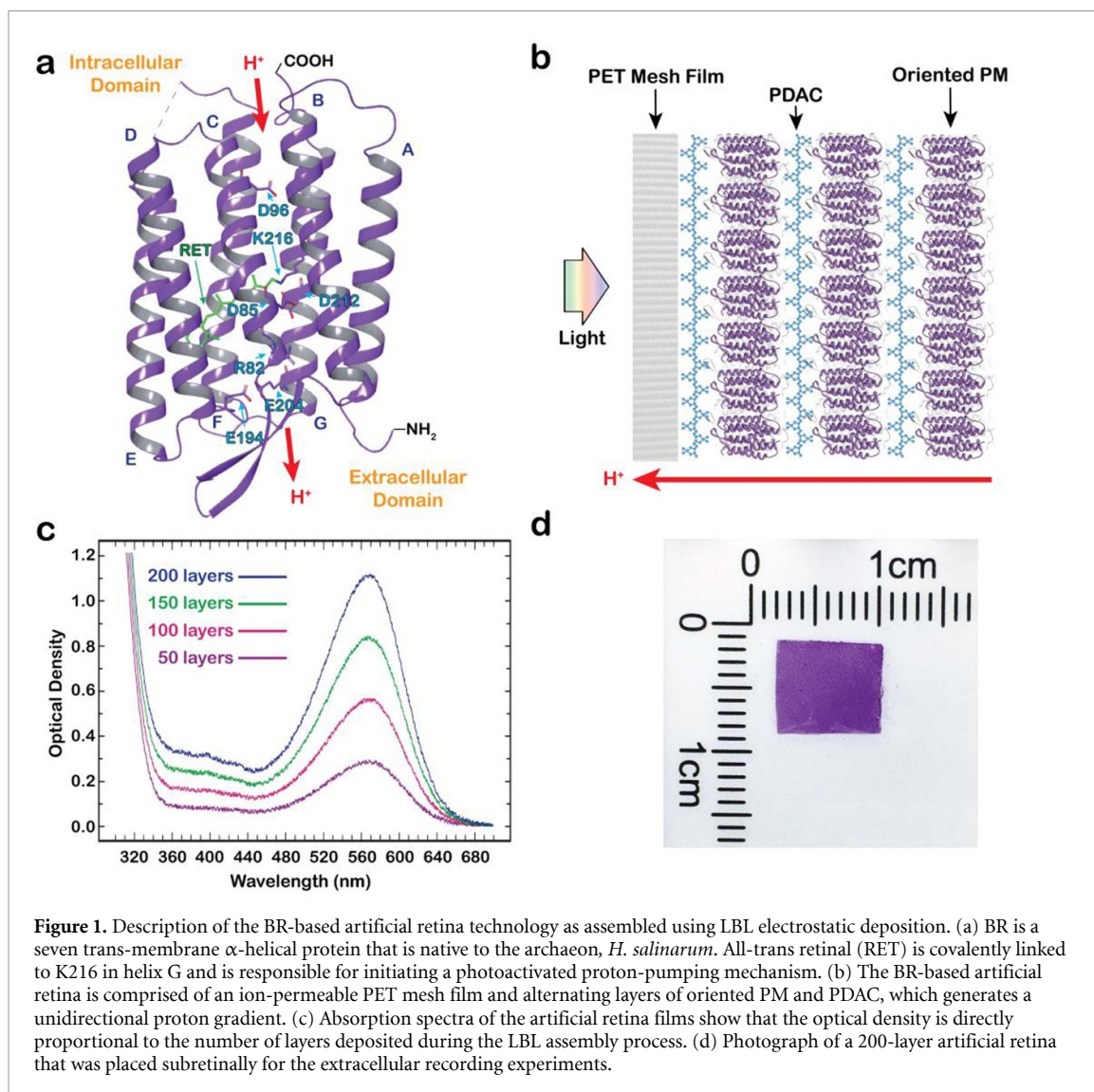


Figure 1. Description of the BR-based artificial retina technology as assembled using LBL electrostatic deposition. (a) BR is a seven trans-membrane α -helical protein that is native to the archaeon, *H. salinarum*. All-trans retinal (RET) is covalently linked to K216 in helix G and is responsible for initiating a photoactivated proton-pumping mechanism. (b) The BR-based artificial retina is comprised of an ion-permeable PET mesh film and alternating layers of oriented PM and PDAC, which generates a unidirectional proton gradient. (c) Absorption spectra of the artificial retina films show that the optical density is directly proportional to the number of layers deposited during the LBL assembly process. (d) Photograph of a 200-layer artificial retina that was placed subretinally for the extracellular recording experiments.

H. salinarum (figure 1(a)). BR-containing PM fractions used within the artificial retina technology originated from the MPK409 cell line of *H. salinarum* (Peck *et al* 2000) and were isolated according to standard procedures (Oesterhelt and Stoerkenius 1974).

2.3. Artificial retina fabrication

The artificial retina prototypes were generated via sequential electrostatic adsorption, achieved through a LBL assembly technique (He *et al* 1998). The three main components of the artificial retina include an ion-permeable scaffold, BR, and a polycation binder (figure 1(b)). The solid support surface of the thin film is a bioinert, ion-permeable mesh comprised of PET microfibers, which has previously been investigated as a material for retinal implants (Scholz 2007). Because the LBL process requires a charged surface for subsequent electrostatic deposition of polycation/protein bilayers, the PET film was first exposed to conditions that facilitate the reduction of surface carbonyl functional groups, which renders the surface negatively charged (Liu *et al* 2007).

Following preparation of the PET-based scaffolding, the LBL manufacturing technique was implemented as first described by He *et al* (1998). The LBL approach utilized poly(diallyldimethylammonium chloride) (PDAC) as a polycation binder between each BR layer. A dipping approach was carried out so that only one surface of the film was coated with alternating PDAC/BR layers. The orientation of the BR on the solid support is such that the plane of the 2D PM lipid bilayer is parallel to the PET film, and the extracellular surface of the PM has been shown to preferentially bind to cationic surfaces (Fisher *et al* 1978), particularly when the net negative charge distribution is enhanced under basic conditions. The process of depositing PDAC/BR bilayers was repeated until the desired number of layers was obtained. The optical density of the BR-based films are directly proportional to the number of layers deposited onto the ion-permeable membrane (figure 1(c)). The films were resized to approximately 1 cm² for the extracellular recording experiments carried out in this study (figure 1(d)).

2.4. Absorption spectroscopy

All absorption spectra were collected using a Varian Cary 5000 UV-visible spectrophotometer (Palo Alto, CA) at ambient temperature. The artificial retina films were inserted into a 1 mm quartz spectrophotometer cell (Starna Cells, Inc.; Atascadero, CA) and the films were suspended in dH₂O. An uncoated PET mesh film in dH₂O was used as the blank for all measurements.

2.5. Animals and tissue preparation

The Institutional Animal Care and Use Committee of the VA Boston Healthcare System (Boston VA Medical Center) approved the studies and ensured the ethical treatment of all laboratory animals. The institution has obtained and is maintaining full accreditation by the Association for the Assessment and Accreditation of Laboratory Animal Care. P23H line 1 homozygous rats were used in this study. The P23H mutation is the most prevalent cause of RP in the US, accounting for about 12% of all autosomal dominant cases of RP. The P23H line 1 rat model is a fast degeneration model of RP (Machida *et al* 2000), in which the rats suffer from a progressive rod degeneration initially associated with normal cone function. Breeding pairs of the P23H-line 1 rats were generously donated by Dr Matthew LaVail (University of California, San Francisco, CA). Each rat was selected to be 6–10 months in age, at which point the majority (>98%) of the photoreceptors were lost (Machida *et al* 2000). The rats were kept on a 12 h light/dark cycle using standard fluorescent lighting (100–200 lux during the light cycle).

On the day of an experiment, a rat was euthanized with sodium pentobarbital (150 mg kg⁻¹, ip) and both eyes were removed and hemisected under ambient room lighting conditions. Following the removal of the vitreous humor from one eye, the retina was gently peeled from the retinal pigment epithelium/choroid and trimmed into a square of approximately 12 mm² using Cohan–Vannas spring scissors (Fine Science Tools, Foster City, CA). The retina was then transferred to a dish containing bicarbonate-buffered Ames' medium (Sigma–Aldrich), and any remaining vitreous was mechanically removed with fine forceps. The retina was then placed photoreceptor side down onto the artificial retina film, and the assembly was then placed in a small-volume (0.1 mL) chamber that was mounted on a fixed-stage upright microscope (Nikon Eclipse E600FN). The mounted P23H retina/artificial retina film was super-infused at 1.5 mL min⁻¹ with bicarbonate-buffered Ames' medium supplemented with 2 mg mL⁻¹ D-(+) glucose and equilibrated with 95% O₂/5% CO₂. A recording temperature of 35 °C–36 °C was maintained using an in-line heating device (Warner Instruments), and the retina was super-infused for at least 20 min before data acquisition. Following the initial removal from the rat, the

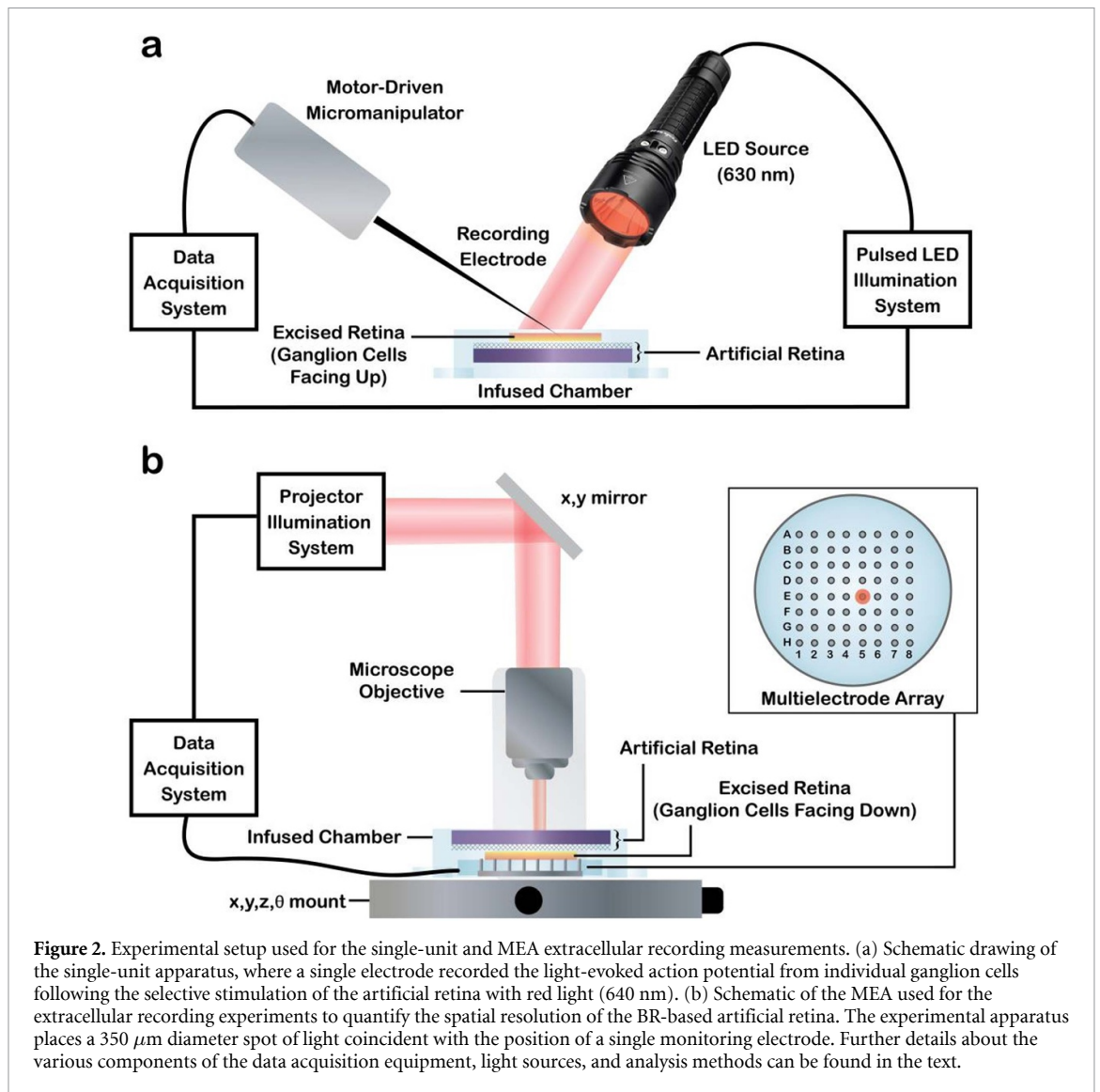
2nd eyecup was transferred to a holding vessel containing bicarbonate-buffered Ames' medium (equilibrated with 95% O₂/5% CO₂) for use later in the day.

2.6. Single-unit electrophysiological recordings

In a dimly lit room, action potentials were recorded extracellularly on individual RGCs using a glass-insulated platinum/tungsten microelectrode (0.6–1.0 MΩ impedance; Thomas Recording GmbH, Germany). With the aid of a red light source (>630 nm) delivered from below the chamber, the tip of the recording microelectrode was visually advanced to the retinal tissue with a motor-driven micromanipulator. Electrophysiological recordings from RGCs were amplified by a differential amplifier (Xcell-3; FHC, Bowdoin, ME) through a bandpass filter (100–5000 Hz). To ensure that recordings were collected from single cells, the recorded waveform of the action potential was continuously monitored in real time to check for uniformity of the size and shape of the waveform. These measurements included both ON and OFF cells, however, the cell types were not distinguished throughout the data analysis. Action potentials from single RGCs were converted to standard transistor–transistor logic (TTL) pulses with a time-amplitude window discriminator (APM Neural Spike Discriminator, FHC). A laboratory data acquisition system (1401 Processor and Spike2 software; Cambridge Electronic Design Ltd, Cambridge, UK) was used to digitize the TTL pulses, and raw action potentials were recorded throughout the experiment. Figure 2 depicts the single-unit extracellular recording apparatus, as well as the multielectrode array (MEA) apparatus described further below.

2.6.1. Light stimulation

Stimulation of the BR-based artificial retina films was accomplished using an in-house precision light source developed for these electrophysiological recording experiments. The illumination device allows one to select one of three Luxeon light emitting diode (LED) light sources (530 nm, 590 nm, and 640 nm). In order to ensure that the signals generated were from the artificial retina and not from the remaining photoreceptor cells, the retina was first bleached with high intensity green light (530 nm, 26.5 mW cm⁻²) for 3 min. Note that rats do not have red cone pigments, and the red-most photoreceptor is the green cone that has an absorption maximum at ~505 nm. The use of this photobleaching step simultaneously light adapts BR for improved proton pumping efficiency. Next, the implant was pulsed with red light (640 nm) to photoactivate BR in the artificial retina films. BR has an absorption maximum at ~570 nm, with which the red LED has a 59 times better coupling efficiency than to the green cone pigment of the rat, as shown in figure 3. Thus, even though the coupling is not ideal,



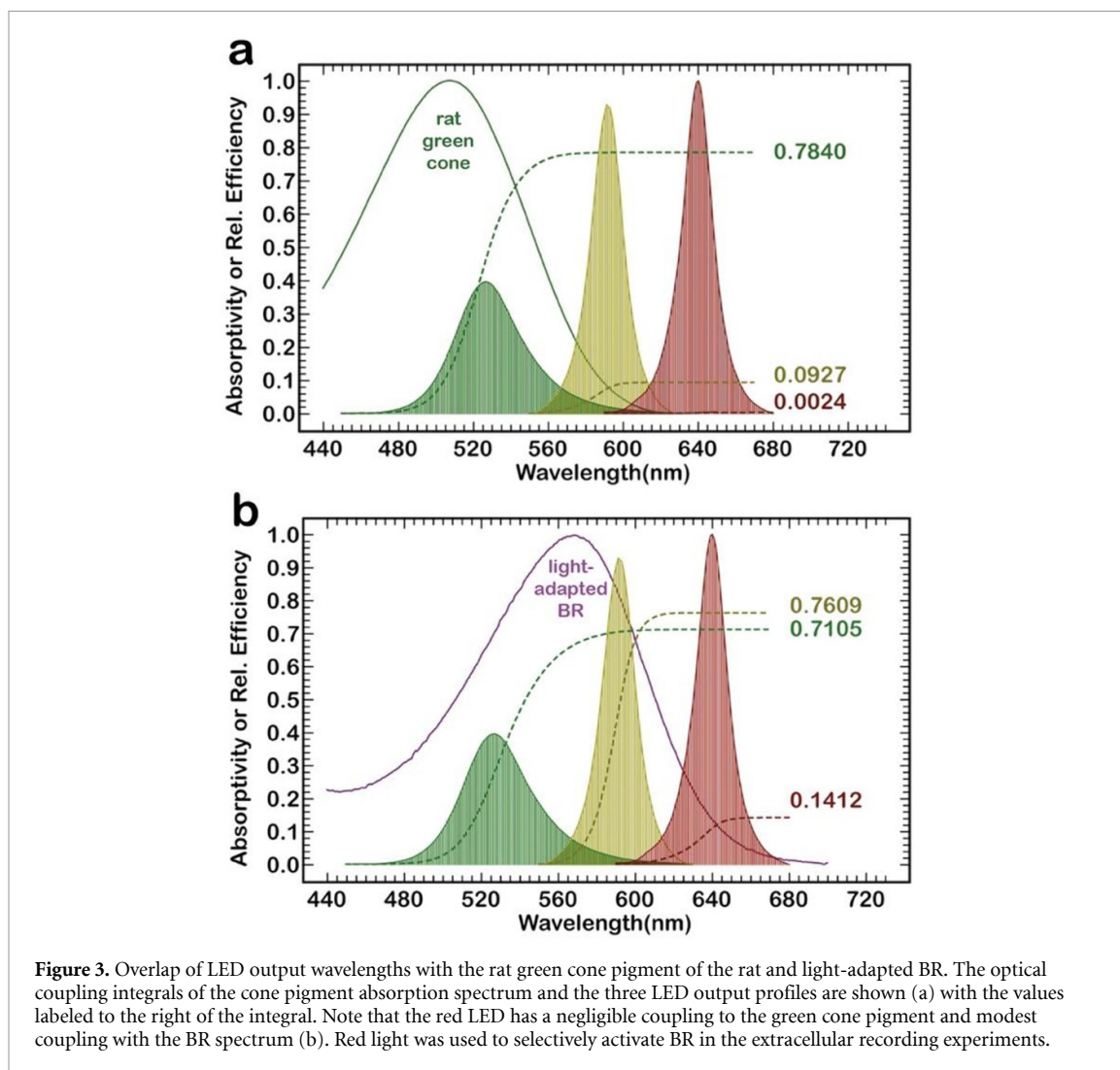
it provides experimental protection against observing cone pigment activation rather than implant-induced activation.

The controller allows manipulation of the light intensity, which is a percentage of the maximum voltage allowed for the LED (3.5 VDC). The intensity of each LED was measured in μJ using a LabMaxTM-TOP laser power/energy meter (Coherent, Inc.) relative to this percentage so that the reported percentage could be translated to an energy per pulse, and ultimately to an effective energy per area. The conversion was done for each LED source and each pulse width, and the measured values shown in figure S1 (available online at stacks.iop.org/JNE/18/066027/mmedia) were fit to a quadratic equation that could be used to convert any percentage power used in an experiment to a corresponding energy value in μJ . These data only apply to a 1 ms pulse width. Separate fits are required for each pulse width to be used because the LED responsivity as a function of pulse width is not linear. Although the pulse energy is nominally measured in μJ , it is more

appropriate to report our results in terms of power per unit area (mW cm^{-2}), which was determined using the LabMaxTM-TOP energy meter, the known pulse width, and the dimensions of the collection area of the EnergyMaxTM sensors (J-10MT-10 KHZ or J-25MT-10 KHZ; Coherent, Inc.). The experiments were first carried out in terms of pulse width (1 ms) and distance of the LED source to the implant (15 cm). Next, we translated the response function to the wavelength maximum of BR rather than the deep red wavelengths that we used to avoid activating any residual rod or cone cells. This process was done for each appropriate experimental condition, wavelength, and pulse width.

2.6.2. Data analysis

The raw action potentials recorded throughout the experiment were acquired and processed using Spike2 software (Cambridge Electronic Design Ltd, Cambridge, UK). The precision in-house LED light source used for illumination of the artificial retinas was integrated into the data acquisition system. The LED



system not only generated a pulse of light, but also a complex TTL trigger sequence that was recorded and included in the data set. These trigger sequences include signatures of the color and power of the LED. Moreover, the relative timing of the last trigger pulse indicates the position of the primary trigger pulse that activates the light pulse. The data files generated through Spike2 were exported and analyzed using in-house software written for MathScriptor (birgegroupp.uconn.edu/software).

In practice, the analysis tabulated the recorded action potentials and counted each observation so long as the peak value exceeds a given threshold value. The activation efficiency is defined as the number of pulses that induce a signal above or below the threshold value during the signal collection period divided by the total number of pulses. If two or more action potentials were observed within the temporal signal region, these spikes only counted as one. Our approach to assigning the threshold value is to generate histogram plots like the one shown in figure S2 and adjust the threshold so that the recovery region peak is roughly 10% of the main peak observed within

the signal region. This approach invariably leads to threshold values of 30–35 μV . The single-unit recordings reported here used a threshold value of 30 μV .

When the action potentials occur relative to the light pulse is as important as the threshold assignment. The temporal response is best observed in the form of a histogram showing all the spikes observed above a given threshold for a sequence of 287 light pulses (see figure S2) as a function of time following the light pulse. We define three temporal regions. The first is the signal region, which starts after a latency of Δt following the light pulse. The value of Δt depends on the P23H rat, the temperature, and the intensity of the light pulse. The stronger the light pulse, the shorter the Δt . We set Δt to 100 ms for most recording periods. The 200 ms long signal region is the temporal region inside of which we count the spikes as valid events. Following the signal region is an inhibition region which is about 50–100 ms in length. The last region is the recovery region which has a length of 600–800 ms. We assign a value of 800 ms to this region to make sure no recovery spike is confused for the signal spike (figure S2).

2.7. MEA electrophysiological recordings

A 64-channel planar Muse MEA (Axion Biosystems Inc., Atlanta, GA), with 30 μm diameter nanoporous platinum electrodes at a 200 μm center-to-center spacing, was used for the assessment of the spatial sensitivity of the artificial retinas (figure 2(b)). The excised retina was mounted on top of the MEA, and the retina was maintained through the carboxygenated Ames' medium conditions described above. The artificial retina was placed on top of the excised retina, oriented such that protons are pumped through the PET mesh film and towards the retina. A piece of porous (30 μm pores) polycarbonate membrane (Stelitech Corp., Kent, WA) and a nylon anchor was placed onto the artificial retina film to hold the assembly in place. The raw data collected by the MEA was digitized at 20 kHz and was stored onto a hard disk for offline analysis.

2.7.1. MEA light stimulation

Continuous incident light was generated with the PsychoPy (v1.81) package (Pierce 2007) delivered through a digital light-processing projector. Images from the projector were minified with external lenses and focused onto the P23H retina/artificial retina assembly with a 10 \times microscope objective. The mean stimulus illuminance was adjusted by neutral density filters positioned adjacent to the projector output, and interference gratings were utilized to select the wavelengths reaching the artificial retina. Green and red interference filters were used to bleach remaining P23H green cone pigments and selectively activate BR, respectively (figure S3). An adjustable aperture was also used to modify the diameter of the light spot that was targeting the MEA. The aperture was capable of permitting the investigation of full-field illumination of all electrodes in the array or targeting the area surrounding individual electrodes. The minimum spot size used was 200 μm at the full width at half maximum, which was coincident with the size and position of a single monitoring electrode within the 64-channel MEA.

2.7.2. MEA data analysis

The spatial sensitivity of BR-based artificial retinas was probed using a 64-channel MEA (Jensen 2017) and by narrowing a continuous beam spot of red light to only activate the area around single electrodes within the MEA (figure 2(b)). The narrowed spot of the red light beam had a diameter of ~ 350 μm and a full width at half maximum equivalent to the separation distance between electrodes (200 μm). All electrodes were monitored simultaneously, and the narrowed beam was translated between adjacent electrodes to evaluate responsivity and receptive field size (Tochitsky *et al* 2014). Sorted action potentials were imported into Neuroexplorer software (Nex Technologies) to quantify the action potentials and firing rate

observed from the illuminated MEA/artificial retina assembly.

An in-house program written using MathScriptor was used to quantify the observed action potentials per recording electrode and calculate the relative activation rate (signals s^{-1}). The firing rate of individual RGCs was calculated relative to the mean firing rate when the retina/artificial retina assembly was in darkness.

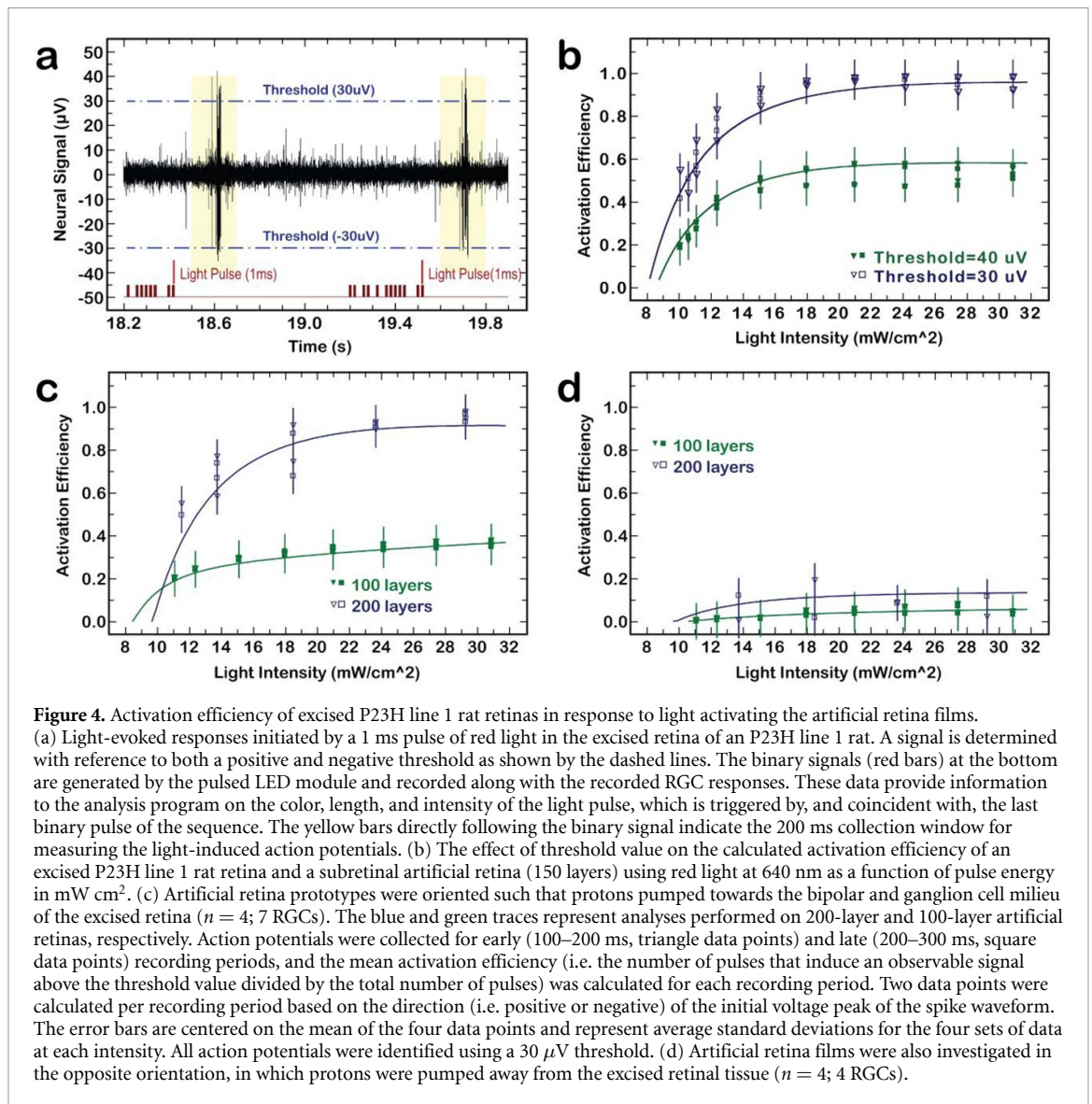
3. Results

3.1. LBL assembly of artificial retina thin films

A mesh film comprised of synthetic PET fibers was used to support alternating layers of BR and a polycation binder, PDAC. The uniform orientation of the protein layers allows for a photoactivated unidirectional ion gradient that is delivered through the apertures of the PET scaffold (figure 1(b)). Artificial retinas of varying numbers of layers were generated for this study to determine an effective optical density to absorb sufficient incident light and generate an appreciable ion gradient to stimulate the P23H line 1 rat retinas. The resulting thin films had a thickness of approximately 80–100 μm and were trimmed to approximately 1 cm^2 , which fully supported the excised retinas for single-unit and MEA extracellular recordings. Figure 1(c) demonstrates an increase in optical density at the absorption maximum of BR (~ 570 nm) as the number of layers are increased on the ion-permeable scaffold. Figure 1(d) shows an example of a 200 layer artificial retina thin film with a surface area of approximately ~ 64 mm^2 , manufactured using the LBL deposition approach described above. Note that the thin film surface area used in these experiments does not represent the thin film geometry intended for *in vivo* applications.

3.2. Activation of RGCs with proton gradients

Ex vivo extracellular single-unit recording methods (Jensen and Rizzo 2011) were used to evaluate the ability of subretinal artificial retinas to stimulate the bipolar and ganglion cells of a degenerated retina from P23H line 1 rats (Machida *et al* 2000). In order to activate the BR-based artificial retina, a pulsed LED apparatus was constructed to generate precise pulses of light with varying pulse energies (~ 7.2 –100 mW cm^{-2}). To ensure that the signals generated were from the implant and not from remaining photoreceptor cells, the retina was first photobleached with green light (530 nm, 26.5 mW cm^{-2}) for 3 min. This step also had the advantage of light-adapting BR (Kouyama *et al* 1985), which improves the efficiency of proton pumping following light absorption. The implant was then pulsed (1 ms pulse width, 1 Hz) with red light (640 nm), which has a relatively high coupling efficiency with BR compared to that of rat green cone pigments (figure 3).



The results presented in figure 4 demonstrate that the BR-based artificial retina was capable of stimulating the retinal tissue. Single RGCs from several regions of each retina were monitored, and an example of the light-evoked responses is demonstrated in figure 4(a). A collection period of 200 ms, following a 100 ms delay time, was used to tabulate the observed action potentials related to the artificial retina stimulation. Activation efficiency was calculated according to the observed signals per pulse of LED light. Setting a $30 \mu\text{V}$ threshold (figure 4(b)) was identified as an effective means to select for light-induced action potentials while excluding those related to noise or spontaneous activity. Figure 4(c) shows that a high activation efficiency was achieved with increasing light intensity for a 200-layer film, whereas the efficiency was cut approximately in half with a 100-layer film. Preliminary evidence demonstrates that 150 layers perform comparably to 200-layer films (figure S4). These observations suggests

that a sufficient number of layers of BR is required to consistently generate an ion gradient that can activate the degenerated P23H line 1 rat retina. Control experiments that decreased $[\text{H}^+]$ by reversing the orientation of the artificial retina generated little to no activation of the neural circuitry (figure 4(d)), which was observed for all artificial retina prototypes with varying numbers of layers.

The series of post-stimulus histograms plotted in figure 5 represent the observed action potentials collected using single-unit recording methods for 200-layer artificial retinas as a function of time following full-field light activation (1 ms pulse, 1 Hz, 640 nm). The histogram analysis showed increasing spike counts with increasing light intensity when protons were pumped towards the retinal tissue, which is similar to the activation efficiency trends observed in figure 4. The average latency of activation for each measured light intensity was approximately 150 ms. In contrast, when the implant was placed in the

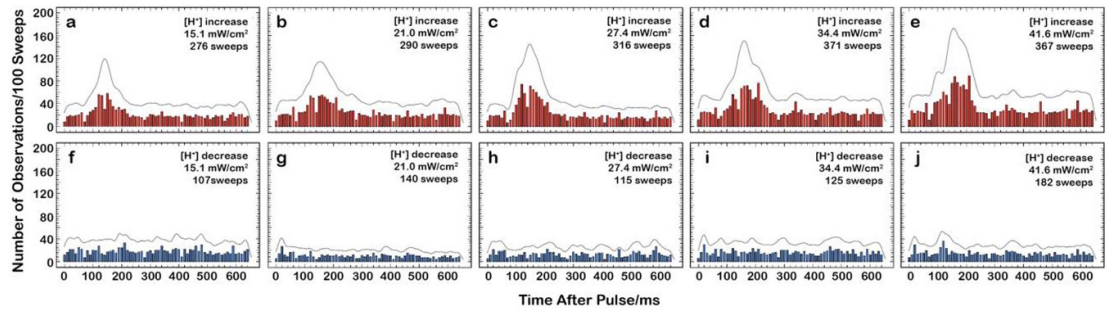


Figure 5. Post-stimulus time histograms of measured RGC action potentials following light activation of the BR-based artificial retina. The top panels ((a)–(e), red) correspond to the case in which the artificial retina is oriented to pump protons towards neural tissue ($n = 4$; 7 RGCs). The bottom panels ((f)–(j), blue) are for the control, in which the implants were placed in the opposite orientation ($n = 4$; 4 RGCs). The y -axis represents the average number of observations of action potentials per 100 sweeps. The offset line plots represent a five-term symmetrical weighted moving average of the action potential counts. A threshold of $30 \mu\text{V}$ was used to tabulate recorded action potentials.

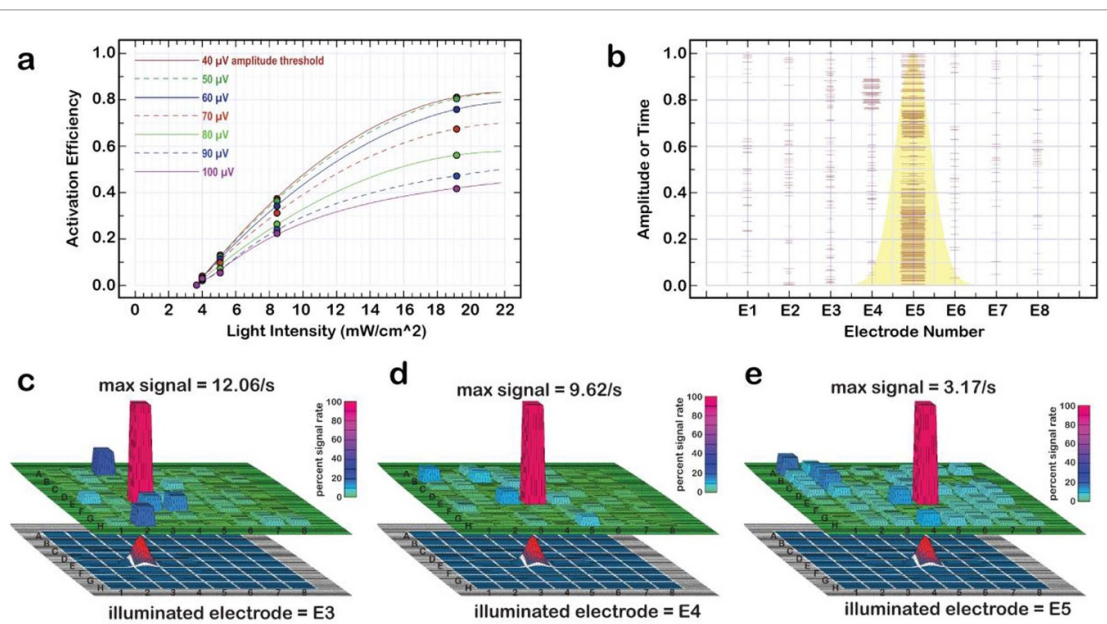


Figure 6. Spatial sensitivity of a 200-layer BR-based artificial retina evaluated using extracellular recording with a MEA on a single P23H line 1 rat retina. (a) The activation efficiency of RGCs by the protein-based artificial retina as a function of light intensity, shown at various amplitude thresholds. The nerve impulses induced by the implant were monitored using amplitude thresholds ranging from 40 to $100 \mu\text{V}$. The spatial resolution analysis shown are performed using a $70 \mu\text{V}$ threshold. (b) Demonstration of selective activation of electrode 5 in row E of the 8×8 MEA. Electrodes E1–E8 are separated by $200 \mu\text{m}$, and the full width at half maximum of the light beam is equal to the electrode separation. The y -axis is the normalized amplitude of the irradiation beam and a normalized time range that spans 110.2 s, which represents a period of continuous illumination. (c)–(e) Targeted illumination of a select region of a P23H rat retina centered on a single electrode within an MEA array, including electrodes E3 (c), E4 (d), and E5 (e), respectively. The upper plot in each panel illustrates the percent signal rate for each electrode throughout an illumination period. The colorimetric legend corresponds to the relative signal rate, and each plot is normalized to the maximum. The lower plot in each panel shows the location and relative beam spot size.

opposite orientation so that protons were pumped away from the retinal tissue, no apparent activation was recorded beyond background noise.

3.3. Spatially precise light responsivity

The spatial sensitivity of the 200-layer BR-based artificial retina was probed using a 64-channel MEA (Jensen 2017) and by narrowing a beam spot of continuous red light (630 nm) to only activate the area around single electrodes within the MEA (figure 2(b)). Based on the single-unit extracellular recording results, the thin films examined using the

MEA were oriented such that protons were pumped towards the bipolar cells of the excised retinas. The single-unit extracellular recording experiments suggested that the relative activation efficiency is dependent on the amplitude threshold that is chosen to monitor RGC activation, and a consistent value of $30 \mu\text{V}$ was used to analyze the single electrode data. Data from the MEA-measured action potentials following activation of the artificial retina using full-field stimulation was analyzed with thresholding from $40 \mu\text{V}$ to $100 \mu\text{V}$ in $10 \mu\text{V}$ increments (figure 6(a)). As expected, lower thresholds exhibited

higher activation efficiency due to signal saturation. At low thresholds, one must also be careful that noise does not contribute to or skew the activation efficiency of the implant. Thus, the spatial resolution analysis discussed below used a threshold of 70 μV , which was found to accurately represent the efficiency.

Figure 6(b) demonstrates the spatial sensitivity by plotting the action potentials throughout a period of constant illumination while electrode E5 in an eight-electrode row was targeted with a narrow beam of light ($\sim 350\ \mu\text{m}$ in diameter) to selectively activate the RGCs in contact with this electrode. The light-activated action potentials measured from the ganglion cells are shown to be localized to this one electrode, with little to no activity observed on adjacent electrodes. Because only targeted neurons in contact with a single electrode showed a light response, we can estimate that the RGC collecting area has an upper limit of 200 μm in diameter. In other words, the ion gradient that was generated is shown to be localized to the illuminated region of the retinal implant.

The targeted activation of the area of an implant around a contiguous set of three electrodes within the MEA is demonstrated in figures 6(c)–(e). Throughout the course of these measurements, the targeted electrode was illuminated with a continuous beam of red light (630 nm), and this beam was translated along row E in the 8×8 MEA. The plots in each panel show the average signal rate (signals s^{-1}) for each recording electrode during a collection period. Note that the maximum signal rates do not directly correlate to temporal resolution (i.e. in frames per second (fps)), due to the potential detection of multiple RGCs making contact with an electrode. When E3 was selectively illuminated (figure 6(c)), the RGC activation was localized to that one spot and was dominated by a high relative signal rate. Some activity was observed by electrodes adjacent to E3, and these events were likely due to a slight overlap with the beam spot onto these electrodes and/or spontaneous activity. Those signals that were measured outside of the illumination diameter were due to spontaneous activity. When the beam spot was translated to adjacent electrodes (figures 6(d) and (e)), the result was reproduced, in which light-induced signals were predominantly identified by the targeted electrode.

4. Discussion

The results of a series of extracellular recording measurements demonstrate that the BR-based artificial retinas are capable of stimulating degenerated P23H line 1 rat retinas when placed in a subretinal orientation, and the putative mechanism of action relies on the generation of a unidirectional proton gradient towards the bipolar and ganglion cell network. We propose that the measured responses of the RGCs are due to the activation of a proton-gated

subgroup of epithelial Na^+ channels (Golestaneh *et al* 2000), known as acid-sensing ion channels (ASICs) (Brockway *et al* 2002, Lilley *et al* 2004). The discovery of ASICs in retinal neurons has identified the potential use of proton gradients to overcome interstitial pH levels ($7.2 < \text{pH} < 7.4$) (Padnick-Silver and Linsenmeier 2002, Lilley *et al* 2004) and directly modulate the activity of these cells (Konnerth *et al* 1987, Waldmann *et al* 1997, Krishtal 2003). The ASICs have a depolarizing conductance that can be activated by protons independent of membrane potential (Ettaiche *et al* 2006). Lilley *et al* demonstrated that the threshold of activation for ASICs in RGCs is pH 6.5, and was able to reproducibly induce action potentials when RGCs were pulsed with rapid, but weak, acidic stimuli on a millisecond time scale (Lilley *et al* 2004). The single-unit extracellular recording results presented here suggest that the artificial retina films are capable of at least generating a localized drop in pH to this level. While the presumed mechanism of action of the artificial retina involves the activation of ASICs in this manner, we cannot rule out that the photovoltaic activity of the protein served as a stimulating mechanism, which was envisioned in original concepts of the therapeutic approach (Chen and Birge 1993). We are currently investigating the proposed proton-mediated mechanism of the multilayered thin films in more detail using pH-sensitive fluorescent dyes and confocal microscopy, while simultaneously investigating the photoelectric response of the films.

The multilayer artificial retina films were shown to induce reproducible RGC action potentials when the subretinal films were oriented such that protons were directed towards the bipolar cell network. The activation efficiency of the 200-layer artificial retina increases with the increasing intensity of incident red light and reaches an efficiency of almost 1.0 at and above $30\ \text{mW cm}^{-2}$, while 100-layer films were significantly less efficient. This result indicates that the optical density of the multilayered films is important for absorbing sufficient incident light and producing a response that can consistently lead to stimulation of the degenerated retina. Throughout the experiment, BR-based artificial retinas stimulated the retina using intensities comparable to indoor ambient light ($\sim 10\text{--}30\ \text{mW cm}^{-2}$). As a comparison, optogenetic technologies utilizing channelrhodopsin-2 have been known to require high irradiance due to low levels of expression and low surface area available for photon absorption, with a required peak intensity of approximately $100\ \text{mW cm}^{-2}$ (Kleinlogel *et al* 2011, Klapoetke *et al* 2014). To reach this level of irradiance in the subretinal space, external light amplification technologies are under development to assist in stimulating optogenetically-sensitized retinal cells (Yan *et al* 2016, Soltan *et al* 2018). Further *ex vivo* and *in vivo* evaluations are underway to determine if our BR-based artificial retina requires light

amplification when in the subretinal space, however, this initial study suggests that the threshold for activation is lower than optogenetic requirements, even when using a red light source with relatively low coupling efficiency with the BR absorption spectrum.

The average latency of RGC activation for 200-layer artificial retinas is ~ 150 ms. This latency is similar to what has been observed for the natural responses of P23H line 1 rat retinas (Jensen 2015), though we can attribute the observed signals to the artificial retina activity due to the dependence on orientation of the films (figures 4 and 5), as well as the difference in light responses based on the number of protein layers (figures 4(c) and (d)). It is also important to note that in other extracellular recording studies, subretinal electrical stimulation has demonstrated a response latency that is more rapid than our observations (Jensen and Rizzo 2006). Because our method of stimulation is reliant on a different mechanism (i.e. the diffusion of ions), we do not necessarily expect similar temporal behavior of our subretinal implant. If we consider the temporal resolution of the artificial retina based on the observed response latencies, these *ex vivo* results predict an approximate resolution of ~ 6 to 7 fps. One limitation of the temporal dynamics is also related to the relaxation time constant of ASICs, which has been shown to be approximately 0.5 s *in vitro* (Lilley *et al* 2004). This response time is long compared to phototransduction and the performance of electrode-based prostheses, though our kinetic observations do not necessarily preclude the achievement of functional visual perception. The interplay between proton gradients and RGC responsivity must be evaluated further.

The MEA experiments characterize the spatial limits of the artificial retina receptive field and validate that lateral diffusion at the interface of the implant and the bipolar cells is minimal. Because neurons near single electrodes of the array were targeted, and because the electrodes are spaced 200 μm apart, the current maximum area of sensitivity is measured at 200 μm in diameter. This resolution is comparable to the Argus II technology (Humayun *et al* 2012), and is lower in resolution than more advanced electrode-based technologies (Lorach *et al* 2015). We predict, however, that our implant is capable of performing at a resolution that is higher than what is demonstrated at the limit of the MEA instrumentation, primarily because pixel dimensions are only limited by packing of protein molecules and the arrangement of apertures on the mesh scaffolds (currently ~ 260 apertures mm^{-2}). A higher density MEA would help to quantify the limits of spatial light responsivity of the artificial retina prototypes with greater sensitivity. While simulations suggest near diffraction limited performance, additional studies are required to verify this prediction.

The results of this work suggest a promising new approach of utilizing BR, a well-studied microbial rhodopsin, within a biomimetic artificial retina architecture to stimulate retinal neural cells. The multilayered implant circumvents some of the inherent drawbacks of ion-mediated optogenetics approaches, including low expression and low optical densities, while still facilitating the light-induced manipulation of extracellular ionic environments. We will continue to utilize *in vitro* and *ex vivo* techniques to characterize the layer-specific activity of the LBL-assembled thin films. Specifically, responses from ON and OFF cells were not independently evaluated in this analysis, and it would be valuable to understand how our ion-mediated mechanism influences resulting optical stimulation patterns. Additionally, ongoing efforts will explore how these data translate to *in vivo* visual acuity and permit the functional restoration of sight for patients that are profoundly blind due to retinal degenerative diseases.

Data availability

The data that support the findings of this study are available upon reasonable request from the authors.

Acknowledgments

Work conducted in the laboratory of R R B was supported by grants from the National Institutes of Health (GM-34548, 1R41 EY023461-01), the National Science Foundation (EMT-0829916), and the Harold S Schwenk Sr Distinguished Chair in Chemistry. Additional grant support was awarded to N L W from the National Science Foundation (Project Grant Numbers: 1448244, 1542456, and 1632465). Financial Support from Fight for Sight (FFS-GIA-18-013.R1) through a Grant-in-Aid award to J A G is gratefully acknowledged. The authors thank L Del Priore (Yale School of Medicine) for comments during the preparation of this article.

Author contributions

J A G fabricated the artificial retinas with design input from M J R, M N S, and D J S. J A G, N L W, and R R B designed the *ex vivo* experiments and analyzed the data. J A G, N L W, and R J J performed the extracellular recording experiments. J A G, N L W, R J J, D B L, and R R B wrote the article.

Conflict of interest

J A G, N L W, and D B L are employees of Lambda-Vision Incorporated, and R R B is the founder of the company.

ORCID iD

Jordan A Greco  <https://orcid.org/0000-0001-7582-9321>

References

- Balashov S 2000 Protonation reactions and their coupling in bacteriorhodopsin *Biochim. Biophys. Acta, Bioenerg.* **1460** 75–94
- Bamberg E, Tittor J and Oesterhelt D 1993 Light-driven proton or chloride pumping by halorhodopsin *Proc. Natl Acad. Sci. USA* **90** 639–43
- Berson E L 1996 Retinitis pigmentosa: unfolding its mystery *Proc. Natl Acad. Sci. USA* **93** 4526–8
- Berthoumieu O, Patil A, Wang X, Aslimovska L, Davis J and Watts A 2012 Molecular scale conductance photoswitching in engineered bacteriorhodopsin *Nano Lett.* **12** 899–903
- Bi A, Cui J, Ma Y-P, Olshevskaya E, Pu M, Dizhoor A M and Pan Z-H 2006 Ectopic expression of a microbial-type rhodopsin restores visual responses in mice with photoreceptor degeneration *Neuron* **50** 23–33
- Birge R R 1981 Photophysics of light transduction in rhodopsin and bacteriorhodopsin *Annu. Rev. Biophys. Bioeng.* **10** 315–54
- Birge R R 1990 Photophysics and molecular electronic applications of the rhodopsins *Annu. Rev. Phys. Chem.* **41** 683–733
- Birge R R et al 1999 Biomolecular electronics: protein-based associative processors and volumetric memories *J. Phys. Chem. B* **103** 10746–66
- Blaurock A E and Stoekenius W 1971 Structure of the purple membrane *Nat. New Biol.* **233** 152–5
- Bogomolni R A, Baker R A, Lozier R H and Stoekenius W 1976 Light-driven proton translocations in *Halobacterium halobium* *Biochim. Biophys. Acta Bioenerg.* **440** 68–88
- Brockway L M, Zhou Z H, Bubien J K, Jovov B, Benos D J and Keyser K T 2002 Rabbit retinal neurons and glia express a variety of ENaC/DEG subunits *Am. J. Physiol. Cell Physiol.* **283** C126–134
- Chen Z and Birge R R 1993 Protein based artificial retinas *Trends Biotechnol.* **11** 292–300
- Chow B Y et al 2010 High-performance genetically targetable optical neural silencing by light-driven proton pumps *Nature* **463** 98–102
- Devine E L, Oprian D D and Theobald D L 2013 Relocating the active-site lysine in rhodopsin and implications for evolution of retinylidene proteins *Proc. Natl Acad. Sci. USA* **110** 13351–5
- Ettaiche M, Deval E, Cougnon M, Lazdunski M and Voilley N 2006 Silencing acid-sensing ion channel 1a alters cone-mediated retinal function *J. Neurosci.* **26** 5800–9
- Fisher K, Yanagimoto K and Stoekenius W 1978 Oriented adsorption of purple membrane to cations surfaces *J. Cell Biol.* **77** 611–20
- Golestaneh N, Nicolas C, Picaud S, Ferrari P and Mirshahi M 2000 The epithelial sodium channel (ENaC) in rodent retina, ontogeny and molecular identity *Curr. Eye Res.* **21** 703–9
- Govindjee R, Balashov S P and Ebrey T G 1990 Quantum efficiency of the photochemical cycle of bacteriorhodopsin *Biophys. J.* **58** 597–608
- Hampf N 2000 Bacteriorhodopsin as a photochromic retinal protein for optical memories *Chem. Rev.* **100** 1755–76
- He J-A, Samuelson L, Li L, Kumar J and Tripathy S K 1998 Oriented bacteriorhodopsin/polycation multilayers by electrostatic layer-by-layer assembly *Langmuir* **14** 1674–9
- Humayun M S et al 2012 Interim results from the international trial of Second Sight's visual prosthesis *Ophthalmology* **119** 779–88
- Humayun M S, Prince M, de Juan E, Barron Y, Moskowitz M, Klock B and Milam A H 1999 Morphometric analysis of the extramacular retina from postmortem eyes with retinitis pigmentosa *Invest. Ophthalmol. Vis. Sci.* **40** 143–8
- Jackson M B and Sturtevant J M 1978 Phase transitions of the purple membranes of *Halobacterium halobium* *Biochemistry* **17** 911–5
- Jensen R J 2015 Effects of dopamine D2-like receptor antagonists on light responses of ganglion cells in wild-type and P23H rat retinas *PLoS One* **10** e0146154
- Jensen R J 2017 Effects of GABA_AR and mGluR1 antagonists on contrast response functions of sprague-dawley and P23H rat retinal ganglion cells *PLoS One* **12** e0189980
- Jensen R J and Rizzo J F 2006 Thresholds for activation of rabbit retinal ganglion cells with a subretinal electrode *Exp. Eye Res.* **83** 367–73
- Jensen R J and Rizzo J F 2011 Effects of GABA receptor antagonists on thresholds of P23H rat retinal ganglion cells to electrical stimulation of the retina *J. Neural Eng.* **8** 035002
- Kandori H 2020 Retinal proteins: photochemistry and optogenetics *Bull. Chem. Soc. Japan* **93** 76–85
- Klapoetke N C et al 2014 Independent optical excitation of distinct neural populations *Nat. Methods* **11** 338–46
- Kleinlogel S, Feldbauer K, Dempski R E, Wood P G, Bamann C and Bamberg E 2011 Ultra light-sensitive and fast neuronal activation with the Ca²⁺-permeable channelrhodopsin CatCh *Nat. Neurosci.* **14** 513–8
- Konnerth A, Lux H D and Morad M 1987 Proton-induced transformation of calcium channel in chick dorsal root ganglion cells *J. Physiol.* **386** 603–33
- Kouyama T, Bogomolni R and Stoekenius W 1985 Photoconversion from the light-adapted to the dark-adapted state of bacteriorhodopsin *Biophys. J.* **48** 201–8
- Krishtal O 2003 The ASICs: signaling molecules? Modulators? *Trends Neurosci.* **26** 477–83
- Lilley S, Letissier P and Robbins J 2004 The discovery and characterization of a proton-gated sodium current in rat retinal ganglion cells *J. Neurosci.* **24** 1013–22
- Liu Y, He T, Song H and Gao C 2007 Layer-by-layer assembly of biomacromolecules on poly(ethylene terephthalate) films and fiber fabrics to promote endothelial cell growth *J. Biomed. Mater. Res.* **81A** 692–704
- Lorach H et al 2015 Photovoltaic restoration of sight with high visual acuity *Nat. Med.* **21** 476–82
- Luo Y H-L and da Cruz L 2016 The Argus® II retinal prosthesis system *Prog. Retinal Eye Res.* **50** 89–107
- Machida S, Kondo M, Jamison J A, Khan N W, Kononen L T, Sugawara T, Bush R A and Sieving P A 2000 P23H rhodopsin transgenic rat: correlation of retinal function with histopathology *Invest. Ophthalmol. Vis. Sci.* **41** 3200–9
- Marc R E, Jones B W, Watt C B and Strettoi E 2003 Neural remodeling in retinal degeneration *Prog. Retinal Eye Res.* **22** 607–55
- Miyasaka T, Koyama K and Itoh I 1992 Quantum conversion and image detection by a bacteriorhodopsin-based artificial photoreceptor *Science* **255** 342–4
- Nagel G, Szellas T, Huhn W, Kateriya S, Adeishvili N, Berthold P, Ollig D, Hegemann P and Bamberg E 2003 Channelrhodopsin-2, a directly light-gated cation-selective membrane channel *Proc. Natl Acad. Sci. USA* **100** 13940–5
- Oesterhelt D and Stoekenius W 1974 Isolation of the cell membrane of *Halobacterium halobium* and its fractionation into red and purple membrane *Methods Enzymol.* **31** 667–78
- Padnick-Silver L and Linsenmeier R A 2002 Quantification of *in vivo* anaerobic metabolism in the normal cat retina through intraretinal pH measurements *Vis. Neurosci.* **19** 793–806
- Palanker D, Le Mer Y, Mohand-Said S, Muquitt M and Sahel J A 2020 Photovoltaic restoration of central vision in atrophic age-related macular degeneration *Ophthalmology* **127** 1097–104
- Peck R F, Dassarma S and Krebs M P 2000 Homologous gene knockout in the archaeon *Halobacterium salinarum* with *ura3* as a counterselectable marker *Mol. Microbiol.* **35** 667–76

- Pierce J W 2007 PsychoPy-psychophysics software in Python *J. Neurosci. Methods* **162** 8–13
- Sahel J-A et al 2021 Partial recovery of visual function in a blind patients after optogenetic therapy *Nat. Med.* **27** 1223–9
- Scholz C 2007 Perspectives on: materials aspects for retinal prostheses *J. Bioact. Compat. Polym.* **22** 539–68
- Singh A K and Hota P K 2007 Development of bacteriorhodopsin analogues and studies of charge separated excited states in the photoprocesses of linear polyenes *Photochem. Photobiol.* **83** 50–62
- Soltan A, Barrett J M, Maaskant P, Armstrong N, Al-Atabany W, Chaudet L, Neil M, Sernagor E and Degenaar P 2018 A head mounted device stimulator for optogenetic retinal prosthesis *J. Neural Eng.* **15** 065002
- Stingl K et al 2015 Subretinal visual implant Alpha IMS—clinical trial interim report *Vis. Res.* **111** 149–60
- Stingl K et al 2017 Interim results of a multicenter trial with the new electronic subretinal implant Alpha AMS in 15 patients blind from inherited retinal degenerations *Front. Neurosci.* **11** 445
- Tochitsky I et al 2014 Restoring visual function to blind mice with a photoswitch that exploits electrophysiological remodeling of retinal ganglion cells *Neuron* **81** 800–13
- Verbakel S K et al 2018 Non-syndromic retinitis pigmentosa *Prog. Retin. Eye Res.* **66** 157–86
- Wagner N L, Greco J A, Ranaghan M J and Birge R R 2013 Directed evolution of bacteriorhodopsin for applications in bioelectronics *J. R. Soc. Interface* **10** 20130197
- Waldmann R, Champigny G, Bassilana F, Heurteaux C and Lazdunski M 1997 A proton-gated cation channel involved in acid-sensing *Nature* **386** 173–7
- Wang W et al 2016 Two-step reactivation of dormant cones in retinitis pigmentosa *Cell Rep.* **15** 372–85
- Yan B, Vakulenko M, Min S-H, Hauswirth W W and Nirenberg S 2016 Maintaining ocular safety with light exposure, focusing on devices for optogenetic stimulation *Vis. Res.* **121** 57–71